Directed networks as a novel way to describe and analyze cardiac excitation: Directed Graph mapping

Nele Vandersickel[a,1,✉], **Enid Van Nieuwenhuyse**[a,1], **Nico Van Cleemput**[b,2], **Jan Goedgebeur**[b,g,2], **Milad El Haddad**[e,2], **Jan De Neve**[d], **Teresa Strisciuglio**[c], **Mattias Duytschaever**[c,e], **and Alexander V. Panfilov**[a,f]

[a]Department of physics and astronomy, Ghent University, Ghent, Belgium
[b]Department of Applied Mathematics, Computer Science and Statistics, Ghent University, Ghent, Belgium
[c]AZ Sint-Jan, Cardiology Department, Bruges, Belgium
[d]Department of data Analysis, Ghent University, Ghent, Belgium
[e]Ghent University Hospital Heart Center, Ghent University, Ghent, Belgium
[f]Laboratory of Computational Biology and Medicine, Ural Federal University, Ekaterinburg, Russia
[g]Computer Science Department, University of Mons, Mons, Belgium
[1,2]Contributed equally

Networks provide a powerful methodology for a variety of biological, technological and social systems, such as analysis of brain data, social networks, internet search machines, etc. Interestingly, directed networks were not yet applied to characterize the excitation of the human heart, although this system would perfect fit for this type of analysis. This is because in clinics, cardiac activation is recorded by multiple discrete electrodes. Their successive excitation in normal sinus rhythm or during cardiac arrhythmia connects neighboring electrodes, and this naturally results in a directed network. In this work, we propose a new concept: application of directed networks to the heart to describe and characterize cardiac arrhythmia. We show that certain tools used in network theory allow us to determine the mechanism and location of cardiac arrhythmia and that the robustness of this approach could exceed the existing state-of-the-art methodologies used in clinics. We demonstrate the proof-of-principle on in-silico and clinical data. Implementing our suggested techniques in the clinic has the potential to improve the accuracy and speed of analyzing cardiac arrhythmia and to provide novel insight in arrhythmia which are still not fully understood.

network theory| cardiac arrhythmia
Correspondence: *nele.vandersickel@ugent.be*

Introduction

A network, in the most general sense, is a collection of nodes connected by links, which can represent diverse systems. Over the past twenty years network theory has proven its merit, from biology to social sciences (1). Examples include the PageRank algorithm (2) for the World Wide Web which formed the basis of Google, determining the shortest route(s) between two places, modelling of molecules (e.g. fullerenes (3)), understanding social networks (4), understanding interactions of genes, proteins, metabolites and other cellular components (5, 6), and the control of the spread of diseases (7, 8). More recently, networks led to the development of novel diagnostic biomarkers in Alzheimer's disease, multiple sclerosis, traumatic brain injury and epilepsy (9). In spite of this diversity, directed networks have not been applied to describe the excitation of the heart. Cardiac contraction is mediated by electrical waves of excitation and abnormal propagation of these waves leads to cardiac arrhythmia. Cardiac arrhythmia remain a major challenge in health care. Among the common types of cardiac arrhythmia are atrial tachycardia (AT), atrial fibrillation (AF), ventricular tachycardia (VT) and ventricular fibrillation (VF). According to the World Health Organization, sudden death resulting from ventricular arrhythmia is still the largest cause of natural death. In recent years, the understanding and the treatment of cardiac arrhythmia has improved due to the ability of recording electrical activity from the endo- or epicardial surface of the heart. The most reliable recordings are made by multiple electrodes placed on the myocardium, which give the local activation time (LAT) of the excitation wave at the discrete points of these measurements. As such, cardiac excitation can be suitable for analysis by network theory, by connecting these locations according to their LAT values.

In clinical arrhythmology it is important to determine the driving mechanism of arrhythmia and its location. There are two main driving mechanisms for cardiac arrhythmia. The first mechanism is reentry, which is characterized by rotational activation. Reentry can be anatomical or functional. Anatomical reentry is characterized by rotation around an obstacle (e.g. scar tissue) and depending on the size of the smallest rotation one divides between macro reentry or localized reentry. Functional reentry is characterized by reentry around an excitable core (often referred to as rotors (10)). The second driving mechanism of arrhythmia is triggered activity or automaticity. The latter mechanism gives rise to focal activation, with most likely a centrifugal activation pattern.

At present, it remains challenging to precisely determine the mechanism of arrhythmia in a given experimental setup or patient. For example, to identify the mechanism of an AT, after ablation of AF, the identification of the underlying mechanism can be complex (11). Moreover, ablation of AF often yields moderate outcomes (12–14). In

the present study, directed networks are used to determine rotational and focal activity with the potential of guiding future ablation strategies. We refer to this method as directed graph mapping (DG-mapping). In a model of chronic atrial ventricular block, we used already succesfully used directed networks to determine the mechanism underlying Torsade de Pointes (15). *However, to goal of this work is to demonstrate the wide applicability of directed networks to the heart for each driving mechanism of cardiac arrhythmia in the atria and ventricles.* Therefore, we tested the accuracy of DG-mapping in in-silico (ventricular) models of functional and anatomical reentry and focal activity. For testing the accuracy of DG-mapping in the clinical setting, we analyzed 31 clinical cases of AT. Regular AT is a clinical tachyarrhythmia in which the operator can be sure about the mechanism and location of the tachycardia. Therefore, AT was used as the gold standard for validating DG-mapping in a clinical setting. In addition, DG-mapping was compared to phase mapping (16) via in-silico simulations, a widely used technique for detecting the center of a rotor.

Results

In-silico models of functional and anatomical reentry and focal activity. The accuracy of DG-mapping was tested in different in-silico models as described in the methods section. First, for functional reentry (see Figure 1A), we simulated a 2D rotor with a configuration of 64 electrodes (A1) and 256 electrodes (A2). In 3D, functional reentry was induced in a simplified model of the ventricles with 64 surface electrodes (A3), and in an anatomical model of the ventricles with 500 intramural electrodes (A4). In all four setups, DG-mapping was able to detect functional reentry and to correctly determine the location of the core of the rotor for the entire length of the simulation (20s duration). The smallest cycle and corresponding core are shown in yellow for each setup. Second, DG-mapping was validated in two models of anatomical reentry (Figure 1B): a 2D anatomical circuit with 64 electrodes (B1) and a 3D anatomical reentry with 500 intramural points in the anatomical model of the ventricles (B2). In both models, DG-mapping correctly identified the reentrant path around the obstacles for the entire length of the simulation (20s). The shortest reentry loops are again depicted in yellow. Third, focal activity was simulated in 2D (64 electrodes) and 3D (500 intramural electrodes) (Figure 1C), by repetitively stimulating 3 different locations. Again, DG-mapping finds the electrodes most closely to the site of stimulation, see C1 (yellow arrows) and C2 (black circles).

Clinical dataset. To demonstrate the proof of concept in the clinical setting, we retrospectively and blindly analyzed 31 cases of regular atrial tachycardia (AT). For clarity, in the supplementary Figure S1, all the steps of the DG-mapping protocol are demonstrated on an AT case of a localized reentry. In general, the atria have a complex structure. During AT, in case of reentry, electrical waves can rotate around the valves, veins or scar tissue. It is important to precisely determine the location of this activation, as the ablation line needs to cut the reentry path so no conduction is possible anymore along that path. The accuracy of DG-mapping was compared to the standard diagnosis i.e. type of arrhythmia and location of the circuit/focal activity as determined by the electrophysiologist (EP) based on the activation map and the ablation result. The overall results are summarized in Figure 2. Out of 31 cases, 20 were based upon macro-reentry, 6 upon localized reentry and 5 due to focal activity, see also the supplementary Table S1. In 9 cases with reentry, the operator was not sure about the mechanism purely based on the LAT activation map and formulated several hypotheses. The gold standard was taken as the diagnosis which matched with the ablation endpoint. Compared to this gold standard diagnosis, DG-mapping identified the exact same mechanism and location in 28 out of 31 cases (90.3%, 95% exact binomial confidence interval 74.2% - 98%). In 3 out of 31 cases, the diagnosis of DG-mapping did not fully match with the gold standard. In 2 cases of double loop reentry, (case 6 and 14), DG-mapping identified only one single loop. In the other case (case 22), the mapping data indicated focal tachycardia, whereas DG-mapping identified localized reentry at the same location. Moreover, in all 3 cases, DG-mapping would have pointed the correct ablation target, meaning that DG mapping correctly identified the ablation target in 31/31 cases.

Representative cases are shown in Figure 3. Panel A depicts a macro reentrant AT around the right veins conducting over the roof. Ablation of the roof resulted in prompt termination of the AT. Blinded analysis by DG-mapping revealed a selected loop at the same location (middle panel). Panel B shows a localized reentry at the anterior wall, rotating around local scar tissue. Ablation from the scar to the mitral valve terminated AT. DG-mapping (middle) as well as wave averaging (bottom) identified the same location of the localized reentry. In panel C, activation mapping and ablation was conform with focal tachycardia at the septum. DG-mapping (in the absence of loops) pointed to focal activity as well (middle panel). We also tested the wave algorithm for each case, as shown in the bottom panels of Figure 3. Wave averaging was compatible with macro reentry (A), localized reentry (B) and focal activation (C).

Comparison with phase-mapping under LAT-variation. In the clinical setup, LAT's might vary due to several factors such as accuracy of the detection algorithms, operator experience, signal quality and noise (17). Therefore, the performance of DG-mapping was compared to phase mapping in the model of a single rotor with 256 electrodes, now with adding Gaussian white noise to the LAT's (Figure 4, upper panels). Overall, we observed that DG-mapping retained its accuracy to detect rotors at increasing noise levels, whereas phase mapping becomes less precise (middle panel of Figure 4): for small variation levels (5 ms), DG-mapping is 100% accurate, while the accuracy of phase mapping decreases to 74.17%. For 15 ms, phase mapping becomes highly unreliable (accuracy of 30.22%), while DG-mapping has an accuracy of 95.49%. For 20 ms, this difference is even more

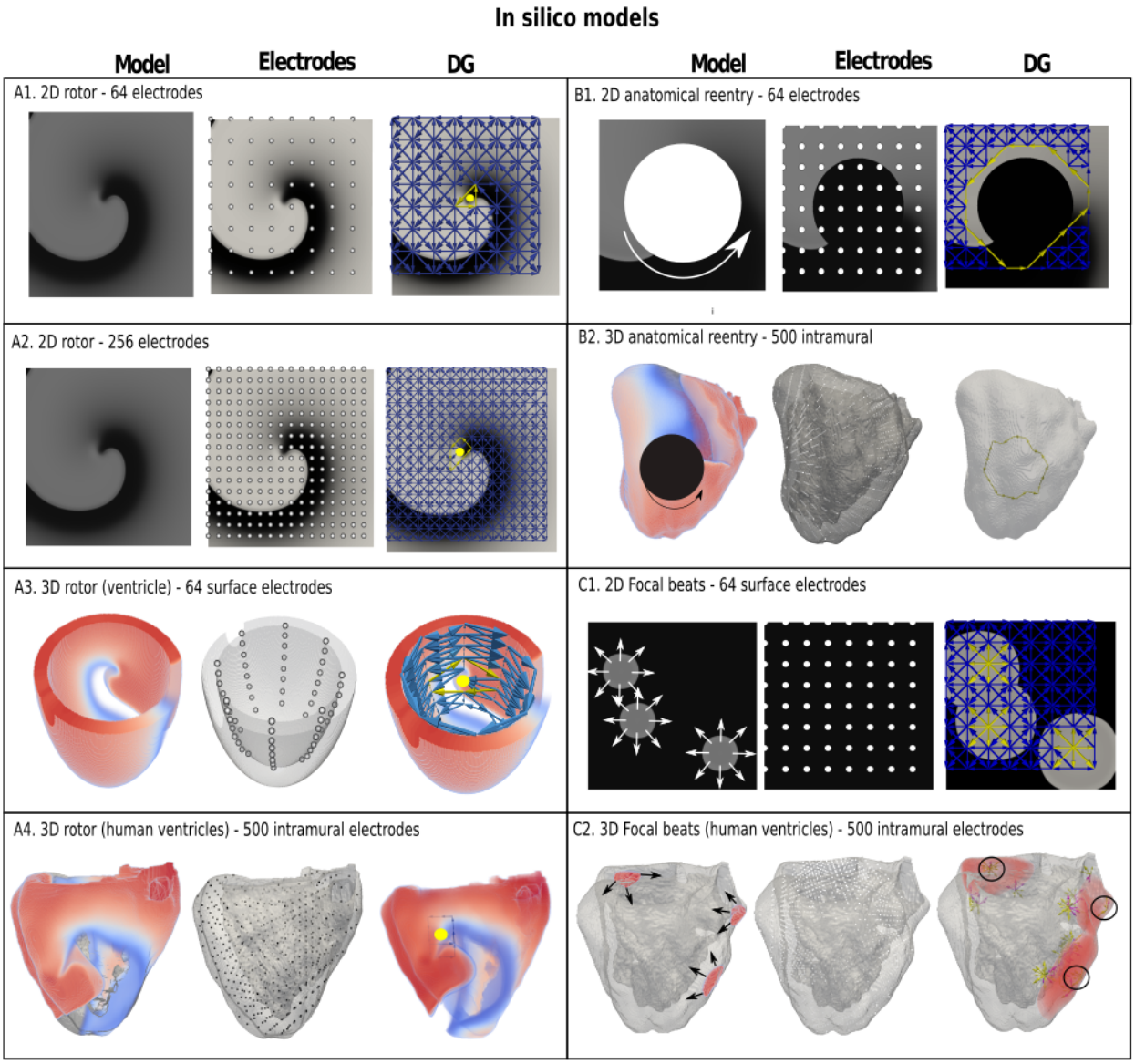

Fig. 1. Examples of DG-mapping for different in-silico models. Model A1 and A2 show a rotor in 2D with 64 and 256 electrodes. Model A3 shows a rotor in a simplified model of the ventricle with 64 surface electrodes. Model A4 depicts a rotor in an anatomical model of the ventricles with 500 intramural electrodes. The smallest cycles and their geometrical centre are indicated in yellow. Model B1 depicts anatomical reentry in 2D with 64 electodes and Model B2 in a model of the human ventricles with 500 intramural electrodes. The smallest reentry loop around the obstacle is again depicted in yellow. Model C1 represents 3 focal sources in 2D with 64 electrodes, whereby DG mapping shows the sources in yellow. Similar results with 3 focal beats in the ventricles are shown in model C2, indicated with 3 black circles. .

pronounced: DG-mapping has an accuracy of 81.19% while phase mapping has an accuracy of merely 1.08% (p-value < 0.0001). Moreover, in case of incorrect diagnosis (lower panels), phase mapping detected extra false cores (type 1 error) whereas in the DG method incorrect diagnosis was due to no detection of the the core (type 3 error). Noise analysis was repeated for the 2D model with 64 electrodes. A similar trend was found with DG-mapping being more accurate (91%, 83%, 68%, for a noise level of 10, 15 and 20 ms) versus phase mapping (75%, 51%, 21%). All of these differences were highly significant (p-value < 0.0001), see also Table S2 in the supplementary material. We also varied the distance to the true core for which we retained a diagnosis as correct, as shown in Figure S2. As explained in the supplementary material, due the discrete nature of phase mapping, we can only compare phase mapping and DG-mapping above a certain threshold. In these cases, DG-mapping always exceeds phase mapping. We also tested the effect of the underlying distribution of the LAT values. Modeling LAT variation with the skewed lognormal distribution did not alter the conclusions of the results, see also Figure S2. Finally, to test the specificity of DG-mapping, we applied DG-mapping in a point simulation model without functional reentry (256 electrodes, LAT variation ranging from 0 ms to 30 ms). In none of the cases, DG-mapping identified a rotor, which resulted in a specificity of 100%.

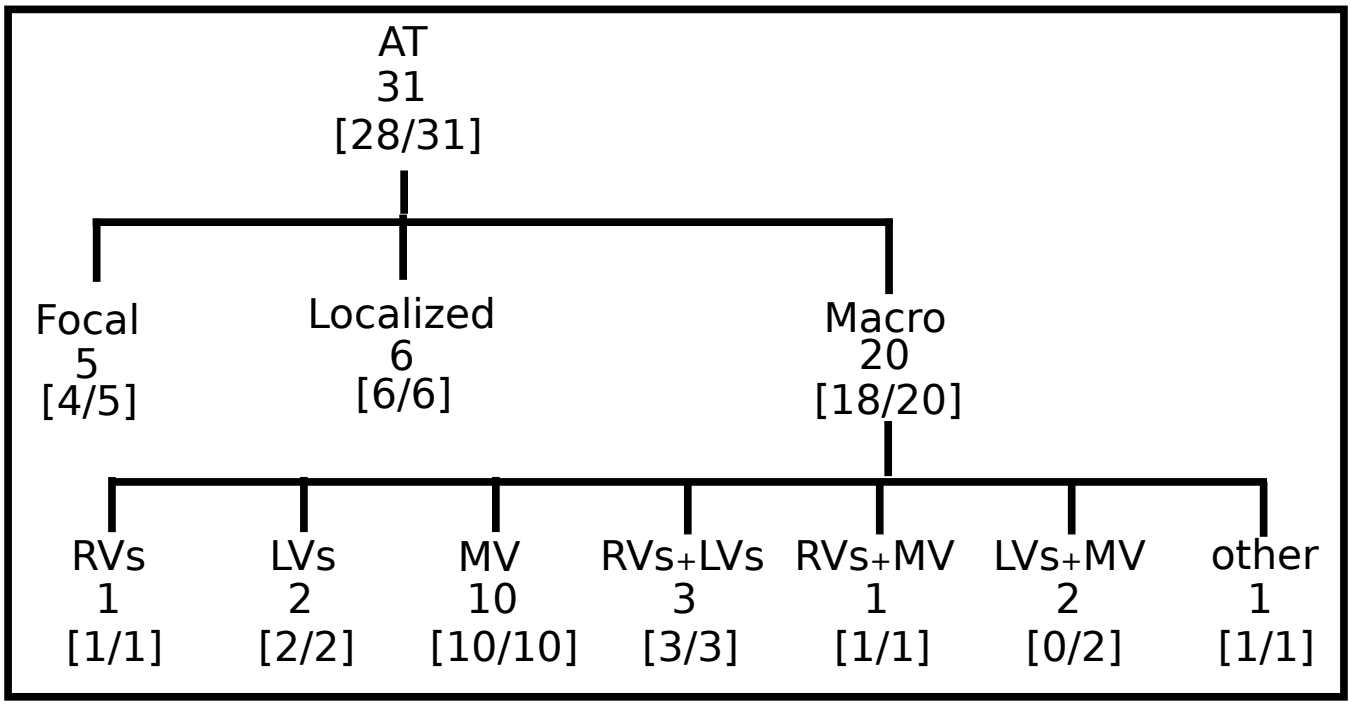

Fig. 2. Accuracy of DG-mapping in clinical AT. The gold standard was compatible with focal source (5), localized reentry (6) and macro-reentry (20). Macro reentry was categorized in reentry around the right veins (RV), the left veins (LV), mitral valve (MV), around RV + LV, around RV + MV, around LV + MV, and other types of reentry (e.g. in the right atrium). In brackets the accuracy of DG-mapping is given.

Region of influence. Describing cardiac excitation as a network, allows to extract additional information. Besides wave averaging, DG-mapping allows to identify the spatial region which is excited by a certain source. In case of normal excitation, a single source (sinus node) excites the whole medium. However, in case of an arrhythmia with multiple sources, each source excites a given region, which we call the region of influence. We hypothesized that DG-mapping, by containing complete spatio-temporal information, can determine this area of influence. This concept was evaluated in 2 different setups (see Figure 5A). We determined the region which contained the electrodes belonging to cycles (region of cycles), as well as the region of influence. Obviously, for a single rotor, the region of influence spans the entire set of electrodes. For 4 different rotors, one can observe an area of influence for each given source.

Discussion

Main findings. We have shown that a geometric directed network can describe electrical activity in the heart in order to find the mechanism of th arrhytmia. This novel method is robust, fast, general, accurate and can be applied to a wide range of in-silico, experimental and clinical models of arrhythmia. First, we have shown that DG-mapping can find functional reentry, anatomical reentry and focal activity in in-silico ventricular models of the heart (see Figure 1). We have tested intramural electrodes, 64-basket electrodes, regular grids with different numbers of electrodes (64-256). We have also tested the DG-mapping om 31 clinical cases of regular AT (atrial cases), see Figure 3. The hypothesis is that this novel method could possibly lead to an improved treatment of cardiac arrhythmia.

Network theory. To our knowledge, so far only limited research focused on network theory to understand cardiac arrhythmia. In the study by Zahid et al. (18), undirected networks were used to find the minimal number of nodes which need to be ablated to separate two regions in the heart. This region is then proposed as the optimal ablation site. In the study by Tao et al. (19), the authors showed that ablation of persistent AF is associated with improvement in both local and global connectivity within the communication networks. However, in neither of the above studies, excitation was interpreted as a *directed* network. Zeemering et al. (20), applied a directed network to describe AF, by accumulating multiple time frames. However, in contrast with DG-mapping, this methodology precluded the possibility of detecting rotational activity, and does not represent the actual wave excitation.

Advantages of DG-mapping. First, we have shown that DG-mapping could be used to reliably detect rotational activity even after adding LAT variation. For instance, in the model presented in Figure 4, we found that in case of 15 ms standard deviation of noise, phase mapping was only 30% accurate, while DG-mapping was still 96% accurate. This difference in accuracy can be explained by the holistic nature of DG-mapping. Even in the presence of a number of electrodes with a wrong LAT annotation, DG-mapping can still identify the correct location of the rotor based upon the other electrodes. In addition, DG-mapping also takes into account the number of cycles which are found for each rotor (with a higher number of loops indicating a higher likelihood for an actual rotation). In contrast, phase mapping finds

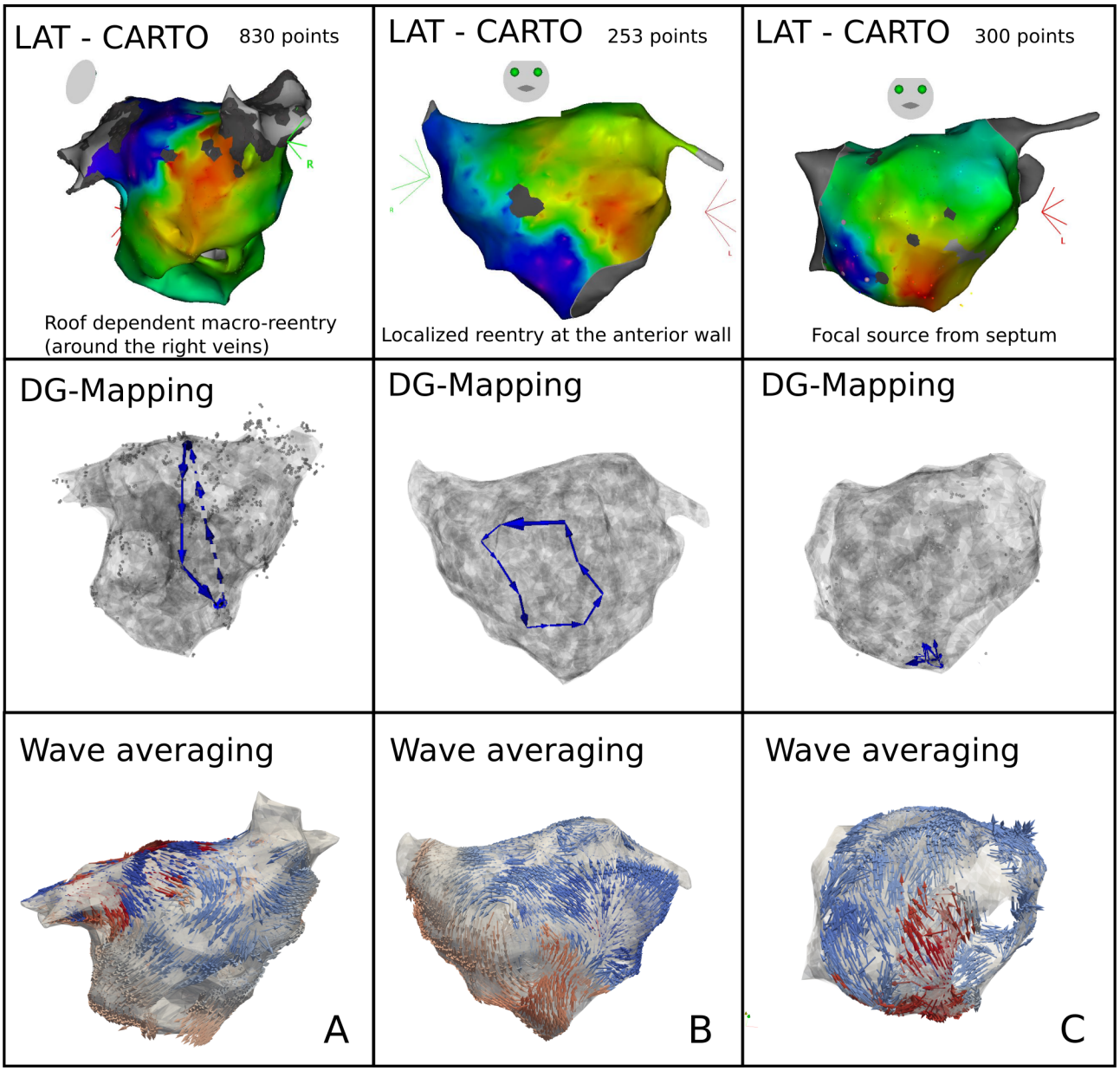

Fig. 3. Representative examples of DG-mapping in 3 cases of clinical AT: macro-reentry (A), localized reentry (B) and a focal source (C). For each case, the activation map and the corresponding DG-map and network based wave averaging is given.

phase singularities locally. Therefore, a misplaced LAT can easily give rise to false positives/negatives, which potentially result in making wrong clinical decisions.

Second, DG-mapping automatically detects anatomical reentry and focal activity, a feature which phase mapping lacks. Very recently, another methodology was described by Oesterlein et al. which can also automatically detect anatomical reentry (21). The approach uses a completely different methodology which is based on integral measures: determining of activated area and its relation to the cycle length of the arrhythmia, while our DG-mapping directly analysis the local propagation of the excitation wave. It would be interesting to compare this method with DG-mapping especially in clinical settings.

Third, DG-mapping offers additional features which can be derived from the directed network. DG-mapping can determine all electrodes belonging to any cycle which are part of the same rotational activity (see Figure 5A), and detect for each rotational core its region of influence (Figure 5B). This offers the possibility to detect all electrodes

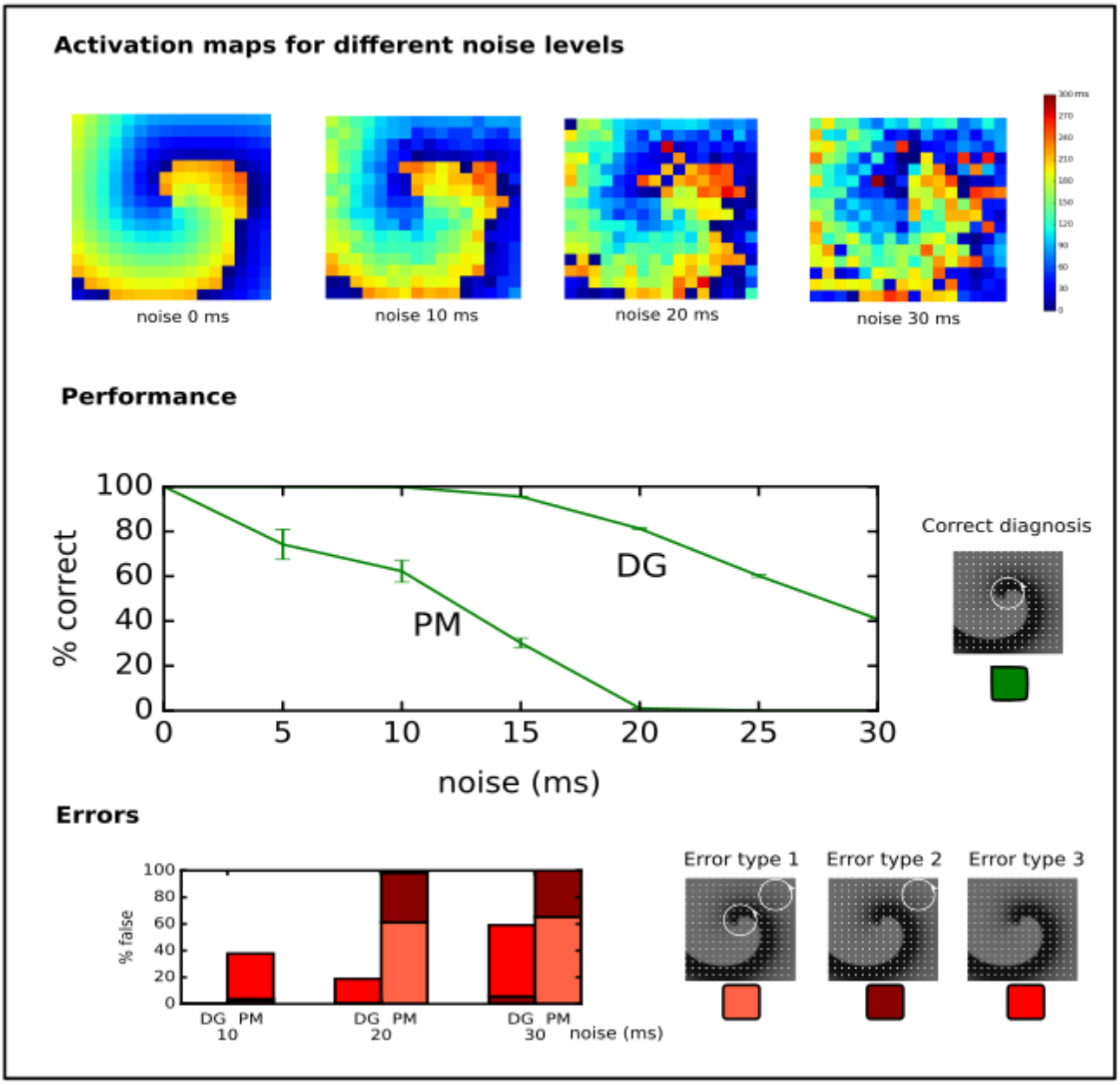

Fig. 4. Performance of DG-mapping and phase mapping (PM) under addition of Gaussian noise with an increasing standard deviation (ranging from 0 to 30 ms) in a single 2D rotor model with 256 electrodes. The upper panels show representative activation maps for different levels of noise. The middle panel shows the performance of DG-mapping versus phase mapping for these different noise level. The bottom panel shows the type of errors in case of failure for both methods. Error type 1 is a detection of a false core in addition to the correct core, error type 2 is only a detection of a false core and error type 3 is no detection of cores at all.

activated by a specific rotational activity, and could detect the dominant driving source of the arrhythmia, the primary target of ablation. Also, the wave averaging technique allows to create maps of the wave propagation, which can provide additional guidance during catheter ablation.

Finally, another advantage is that DG-mapping can be applied to any type of recording system, with varying number of electrodes, the inter-electrode distance or site of recording, as shown in Figure 1.

Clinical implications. DG-mapping could be of added value in the ablation of regular AT. Despite improvements in activation mapping (RHYTHMIA by Boston Scientific, Coherent mapping system by Biosense Webster), interpretation of activation maps remains challenging and operator dependent. We demonstrated that DG-mapping automatically identified the same mechanism as the EP in 28/31 cases of regular AT, but did find the correct ablation target in 31/31 cases. Moreover in 9 cases with reentry, the operator was not sure about the mechanism based on the

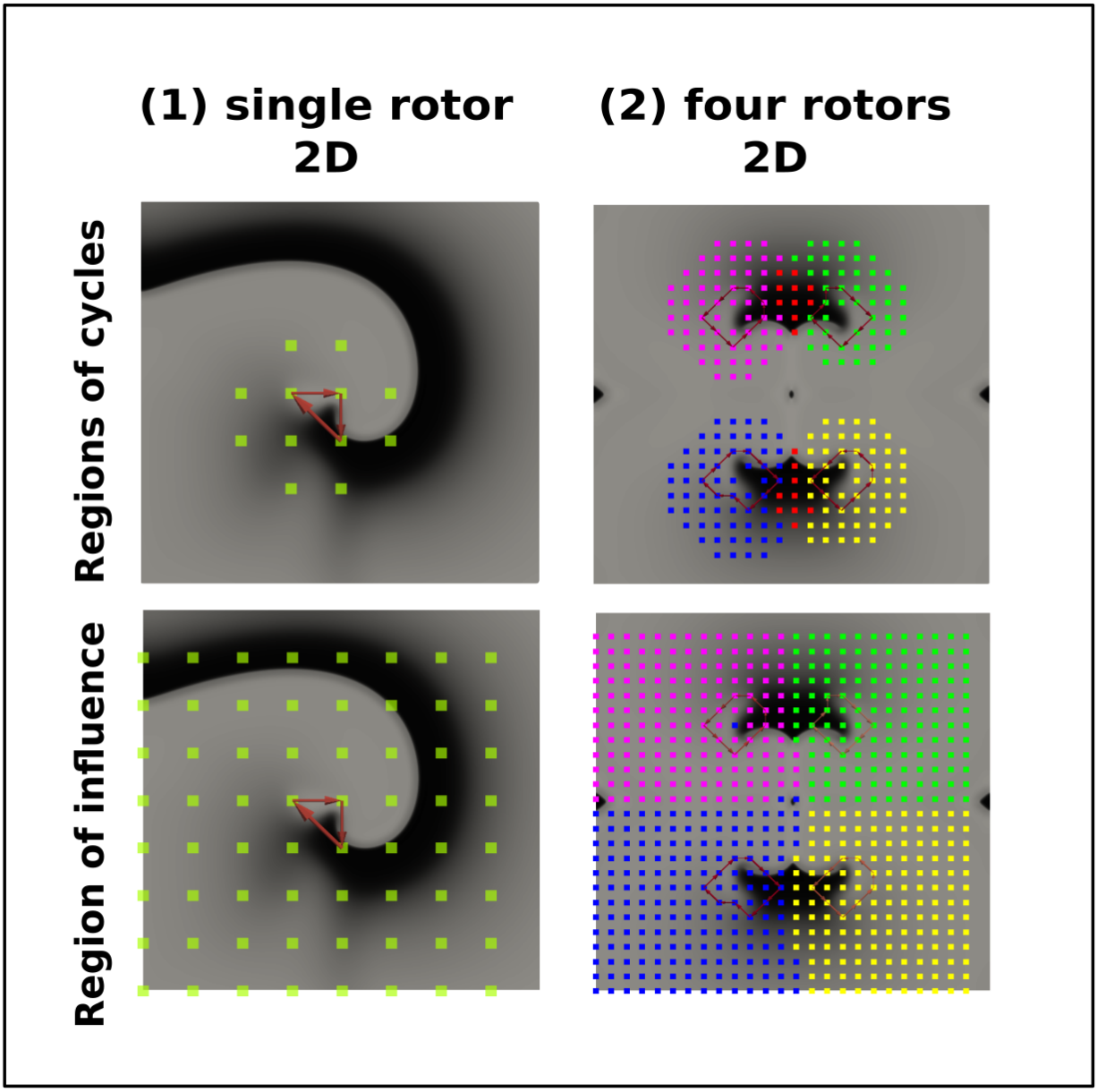

Fig. 5. The regions of cycles and the regions of influences for model A (single rotor) and model B (four rotors). Model A and B were simulated with 64 resp. 625 electrodes. The smallest cycles are depicted in red. Different regions of cycles were depicted in different colors, while the overlap is shown in red. Similarly, different regions of influence are shown in different colors, dividing model B into four different regions.

LAT activation map and formulated several hypotheses (see supplementary Table S1). Currently, in case of doubt, the operator can perform entrainment mapping whereby the post pacing interval (PPI) is compared with the tachycardia cycle length (TCL) to localize or confirm the correct reentry circuit (22) (i.e. where the PPI is equal with the TCL). Therefore, DG-mapping could aid physicians in finding the correct diagnosis according to the ablation target. In addition, DG-mapping also automatically detects focal activity and its location, which makes DG-mapping a complete diagnostic tool for AT. Also, the wave averaging technique allows to create maps of the wave propagation, which can provide additional guidance during catheter ablation.

Another important clinical application is AF. AF is often referred to as the most common arrhythmia in clinical practice with an estimated prevalence of 2% and is associated with a five-fold and two-fold higher risk of stroke and death, respectively (23). Catheter ablation of AF yields moderate success rates (12–14), which is related to the lack of understanding of AF mechanisms. Different mechanisms for AF have been described such as focal activation, dissociated

activity or stable rotors (24–29). Currently, both researchers and electrophysiologists rely on activation mapping or phase mapping for the analysis of AF. Recently, initial studies suggested good outcomes after ablation of rotors guided by phase mapping (30, 31). However, new studies emerged contradicting this study (32–34). It was shown that phase mapping easily generates false positives (35, 36), especially due to LAT variations on the signals and large inter-electrode distances. It remains to be seen whether DG-mapping will offer new insight in AF mechanisms, however, the holistic nature of the method (as explained in the advantages of DG-mapping) might overcome the problems with phase mapping, as currently used in the clinic.

Another possible application is VT, whereby network theory could be used to analyze the substrate during sinus rhythm, as VT are usually hemodynamically unstable and cannot be mapped during VT (37).

In conclusion, translating cardiac arrhythmia into directed networks as described in the current work offers the beginning of a new area of research. There exists a whole range of different algorithms from network theory (such as edge density, centrality measures, etc. (38–41)), which can possibly be applied to the constructed networks to increase our understanding of cardiac arrhythmia.

Limitations. As this paper was a proof-of-concept, many different settings are not yet tested. For example, it is not clear how DG-mapping will work during AF and VT.

Material and Methods

In the next sections we explain the general protocol of DG-mapping, see Figure 6.

Input. The DG-protocol can be applied to a wide range of in-silico, experimental and clinical models of arrhythmia with different types of electrode systems (e.g. basket electrode system, intramural needle electrodes, high density grid data, unstructured electrodes systems,...). We will demonstrate this with in-silico generated and clinical data.

In-Silico generated datasets. All simulations were done with the TNNP-computer model for human ventricular cells (42) by using the explicit-Euler integration scheme (43) on a GeForce GTX 680 and a GeForce GTX Titan, with single precision. We simulated the following different scenarios: (1) Functional reentry was simulated in 2D (in a domain of 512 by 512 grid points with inter spacing of 0.25 mm) and 3D (a simplified model of the human ventricle and an anatomical accurate model of the human ventricle (44)). (2) Anatomical reentry was also simulated 2D and 3D (anatomical model of the human ventricle). For both scenarios, the S1S2-protocol was applied to obtain rotational activity (45). (3) Focal activity was simulated in 2D and 3D (anatomical model of the human ventricle) by applying 3 stimuli at 3 different locations each 500 ms. All simulations were performed for a duration of 20s.

For each different setup, we implemented either 64 surface electrodes (mimicking 64 electrode-basket catheters (30)), 256 surface electrodes with an interspacing of electrodes of 0.8 mm (mimicking experimental grid sizes (46)), or 500 intramural electrodes (in the 3D anatomical model) in analogy with the experimental setup by Taccardi et al. (47) For these electrodes, we computed local unipolar electrogram (U-EGM) as follows:

$$ECG(t,\vec{x}) = \frac{\int \vec{\nabla} V(t).(\vec{r}-\vec{x})}{|\vec{r}-\vec{x}|^3} d\vec{r} \qquad \textbf{(1)}$$

where t is time, x is the distance to the tissue, V is the transmembrane potential, r is the integration parameter over the tissue. The XYZ-coordinates of the selected electrodes were also stored for further analysis. The LAT of each electrode was determined by taking the steepest negative slope $(-dV/dt)$ of the calculated U-EGM. This coincides with the upstroke of the action potential (i.e., the true moment of activation) (48, 49).

Clinical datasets. Between April and August 2017, 29 patients undergoing ablation of symptomatic ATs at AZ Sint-Jan Bruges Hospital were enrolled in the study. The study was approved by the local ethical committee of Sint-Jan Hospital Bruges. High density ($>$ 300 points) endocardial mapping of ATs was performed with a single-electrode mapping and ablation catheter with a distal 3.5-mm tip and three 1-mm ring electrodes (THERMOCOOL SMARTTOUCH Biosense-Webster Inc., Diamond Bar, CA, USA). The bipole of a decapolar coronary sinus (CS) catheter was selected as reference for activation mapping (i.e. peak of CS = 0 ms). The following settings for activation mapping were applied: mapping window set to tachycardia cycle length minus 10 ms and centered at the 0 ms reference, minimum contact force of 4 g, LAT stability of 10 ms, respiratory gating enabled, and color fill calibrated at 5. Bipolar scar threshold was defined at 0.05 mV, and EGMs with bipolar voltages lower than this cutoff will therefore be automatically tagged as scar (gray zones) on the activation maps.

Automated and continuous acquisition of points was done by the CONFIDENSE mapping module (Carto 3 v. 4, Biosense Webster Inc.) using the novel hybrid LAT annotation method (LATHybrid) (50). Each AT case was analyzed off-line by DG-mapping after exporting all local activation times (LATs) and the corresponding 3D coordinates.

The tachycardia mechanism was confirmed when ablation resulted in sinus rhythm or in conversion of a second tachycardia.

Directed graph mapping protocol. This section explains the DG-mapping algorithms, see Figure 6.

Determine the neighbors in a given system. First, for a given configuration of electrodes, for each electrode its possible

neighbors are determined. These neighbors cover all possible paths where the wave can travel starting from a certain electrode. For regular grids, the neighbors are found by setting a spheric distance around a single point. Hence, a single point incorporates maximally 8 neighbors in case of the 2D grid, and maximally 26 neighbors in case of a regular 3D grid. For an irregular configuration of electrodes, like the clinical AT cases, Delanauy triangulation is applied to determine for each electrode its possible neighbors. For example, in Figure S1A, we plotted all possible neighbors for a certain electrode in space for a case of regular AT.

Create network of cardiac excitation. We chose a certain time t. Starting from this time, we find $LAT_1, ..LAT_n$ which are the first LAT larger than t for each electrode in our system of n electrodes. We then draw arrows as follows (15). Suppose electrode 1 and 2 form a pair of neighbors. Assume electrode 1 has LAT_1 and electrode 2 has LAT_2, with $LAT_2 > LAT_1$, meaning the difference between the two electrodes is $\delta LAT = LAT_2 - LAT_1 > 0$. We allowed a directed link from from electrode 1 to 2 if (15):

$$CV_{min} < \frac{\delta d}{\delta LAT} < CV_{max}. \quad \textbf{(2)}$$

In this equation, CV_{min}, CV_{max} and d represent minimal conduction velocity, maximal conduction velocity and the euclidean distance between the two electrodes respectively. For the simulated examples for ventricular tissue (2D and 3D) we took $CV_{min} = 0.2mm/ms$, and $CV_{max} = 2.00mm/ms$. For the clinical AT cases, CV_{min} was set at 0.08 mm/ms, according to the lowest physiological conduction velocity in human atria determined by Allessie et al. (51), CV_{max} was set to maximal 2.0 mm/ms (**?**). In any case, we always tested our result for different values, which resulted in stable loops in large parameters ranges.

Once this first graph was created, a second graph, graph 2, at a time $t + \delta t$ was created in exactly the same way as the first graph. We set $\delta t = 40$ ms. Finally, these two graphs were merged. The resulting graph is the final directed network. For example, in Figure S1B-C, we plotted the resulting arrows from a single node and the complete network for a case of regular AT.

Rotational activity. Once the network is created, any type of rotational activity can be found by detecting cycles in the network. A cycle is a closed directed walk without repetition of nodes. In order to find the cycles, a standard breadth-first search algorithm was used. Since the constructed network in general turns out to be rather small and very sparse, this can be done very efficiently. A first version used bounding criteria to only detect the globally smallest cycles (up to some tolerance), but it turns out that even detecting all smallest cycles through each node can be done almost instantaneously. We ran theoretical simulations on networks with 1 000 000 nodes, and even in these cases all cycles were found in the range of seconds. Clearly, the physical bounds on the number of electrodes that can be placed will be more limiting than the computational work that is needed to process the data. In Figure S1D, the resulting cycles of the network of a regular AT case are shown.

In order to find the core of any type of rotational activity, we looked for the smallest cycles in the network, and computed its geometric center. This was done by grouping all found cycles based on the proximity of the geometric center. If the centers lie closer to each other than a specified threshold, the cycles were considered to belong to the same core. Afterwards there was an optional pass which merges bundles of cycles if they shared nodes. Finally, the centers of each bundle were output as the core of rotational activity. In Figure S1E, the selected cycle is shown. In addition, the corresponding LAT map is also shown in Figure S1D.

Focal activity. Focal activity was detected as a source node, i.e., a node which has a non-zero out-degree, and an in-degree equal to 0. These can be found immediately by doing a single pass over all nodes. Then, the LATs were bundled in certain intervals, to reduce the inter-variability in the LAT values. Afterwards, we reconstructed the network with these bundled values. We then checked if regions with only outgoing arrows were present. The middle of these regions corresponds to the source of the focal activity.

Additional features of network theory. In addition finding rotational and focal activity, we derived additional properties of the network.

Region of influence. For each network containing rotors, we can determine a 'region of cycles' and a 'region of influence'. The region of cycles contains all nodes (electrodes) which are part of cycles for a particular rotor. Second, for each non-marked point we can determine the closest 'region of cycles' in terms of network arrival time distance and related it to that region. As a result, for each point we can determine which source excited it. This is called the 'region of influence'.

In order to construct the region of influence the following algorithm was implemented. For a given network, all n cores were determined, $c_1, ..., c_n$. For each core, we first determined all nodes which are part of cycles of the network ($C_1, ..., C_N$), i.e. the regions of cycles. Then, each node was added to the core c_i to which it had the shortest path to one of its nodes in C_i. In this way, each core is assigned a region of influence.

Wave averaging. Another application of the constructed network is wave averaging to interpret the cardiac excitation pattern. In general, wave averaging consists of decomposing any directed link into smaller arrows which are each projected on a given 3D geometry, followed by averaging all arrows within 1 cm of a node. In more detail, the following steps are taken in the wave averaging algorithm. First, each LAT-node was projected on the mesh. Second, each arrow of the directed network was also projected on the mesh in the following way:

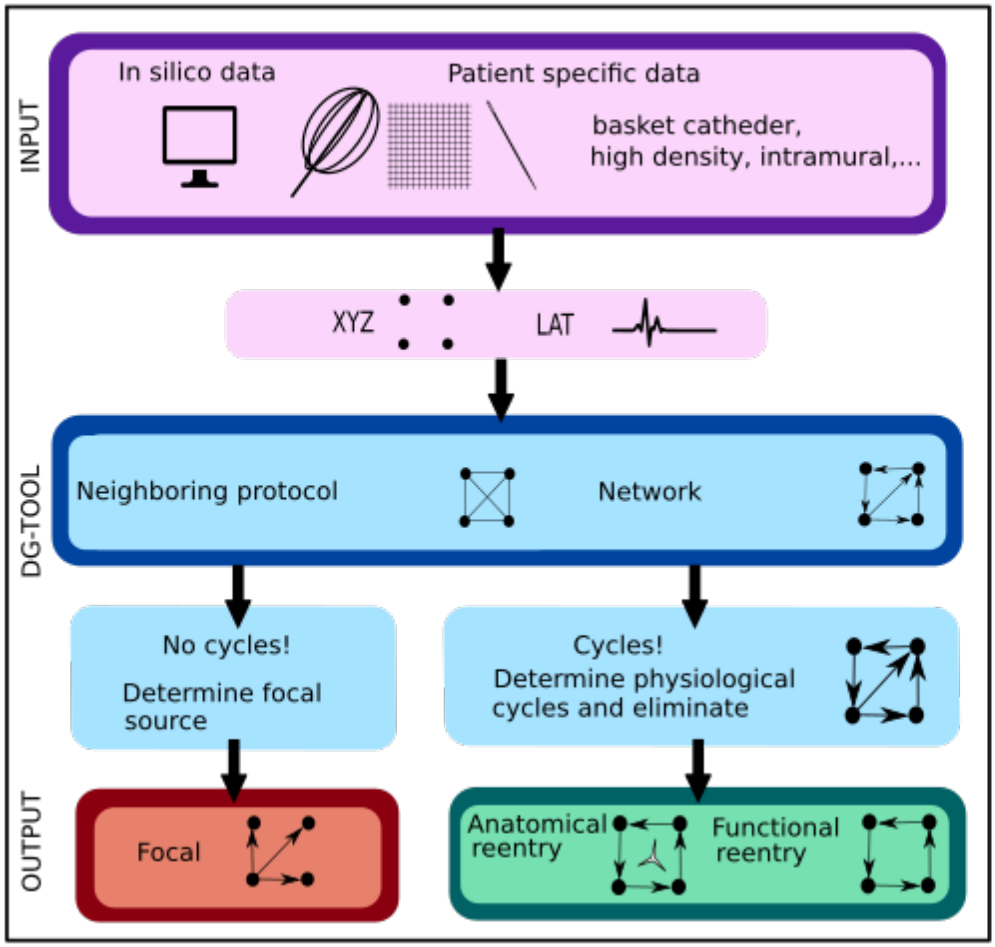

Fig. 6. Illustration of the work flow of the DG-mapping tool. As input, the DG-tool requires for a given setup of electrodes the LAT values with the corresponding XYZ coordinates, which can be extracted from either simulation studies or a clinical setup. The input is then processed as follows in the DG-tool. First, for each electrode a neighboring protocol is applied to identify its neighboring electrodes. Second, the network of excitation is generated. Next, we apply a loop-finding algorithm to detect cycles in the network. If cycles are not detected, we locate the source of focal activity. In case cycles were detected, the loops are merged and its center is determined. At the end, the output is visualized. In case of a focal source, arrows pointing away from a (group of) node(s) are shown, while for reentry, arrows will be plotted to visualize the reentry path.

(A) Each arrow $\vec{x}$ between two LAT-nodes on the mesh was divided in two arrows, both projected on the mesh, $\vec{x}_1, \vec{x}_2$. (B). Each of these arrows $\vec{x}_1, \vec{x}_2$ is then again divided into two arrows and projected $\vec{x}_1 \rightarrow \vec{x}_{1a}, \vec{x}_{1b}$ and $\vec{x}_1 \rightarrow \vec{x}_{2a}, \vec{x}_{2b}$. Therefore, one arrow $\vec{x}$, was divided in 4 projected arrows on the mesh $\vec{x}_{1a}, \vec{x}_{1b}, \vec{x}_{2a}, \vec{x}_{2b}$. Third, for each node n on the mesh, each directed arrow starting from this node as well as each connection of each node within 1 cm from the original node n was averaged. The collection of these averages was then plotted on the mesh.

Phase mapping protocol. LAT values were used to construct the excitation patterns in phase-space. First, a sawtooth wave, with amplitude ranging from $-\pi$ to π is constructed based on these LAT values. Afterwards, values are adapted with their 2π equivalent within the range of $-\pi$ to π in phase-space. Next, in both x and y direction, the phases were derived and a linear combination with the Sobel (we also tested the Nabla) kernels to detect the singularities was applied. This protocol was previously presented (52–56), but instead of the Hilbert transform we made use of the sawtooth wave for the phases. In 3D, the heart was sliced in 3 orthogonal directions and the protocol was applied on each slice. However, as the shape of the ventricle model is complex, only grid points with complete circumference in the heart were taken into account, so convolution did not result in false positives on the edges (57). However, this did not result in detection of the filament of the rotor as the density (500 intramural points) was too sparse. We therefore calculated the phase singularities on the surface of the tissue and detected eventually the phase singularities of the spiral in 3D. A binary detection threshold was applied to the convolution (56), set to 95% of the maximal detected value in phase-space.

Introducing LAT variation. In the clinical setup, identification of LAT whether by automated algorithms or manual an-

notation by operators might vary due to several factors such as accuracy of the detection algorithms, operator experience, signal quality and noise (17). Therefore, we included LAT variation in our analysis, and compared the accuray of DG-mapping with phase mapping. LAT variation was obtained by adding random Gaussian noise to the LATs with standard deviations $\sigma = 5, 10, 15, 20, 25, 30$ ms in the simulation of functional reentry with a configuration of 64 and 256 electrodes. For this, we divided the activation times obtained during a simulation in 25 different frames with 520 ms separation to exclude any overlap in activation times. For each frame, we randomly added Gaussian noise 1000 times, so in total, we compared 25000 different frames per LAT variation σ. Then the center of the rotor was detected with DG-mapping and with phase mapping. For DG-mapping, the geometric center of all cycles belonging to the same core was computed. Afterwards, the median value was taken as the true center of the rotor. In addition, only the center with the highest number of cycles was taken into account. We classified the outcome as correct if only one single core was found within 1.0 cm of the true core. The incorrect diagnosis was classified in 3 different types: incorrect cores (i.e. cores outside a 1.0 cm radius of the true core) in combination with the correct core (error type 1), only incorrect cores (error type 2), or no cores (error type 3). For the percentage correct diagnosis p, we computed a 95% confidence interval via $p \pm 1.96SE$ where SE is obtained from a robust sandwich estimator (58, 59) that accounts for the correlation structure (i.e. the 1000 replicates within one time frame are expected to be correlated). In the supplementary material, we also simulated noise from the skewed lognormal distribution to study the robustness of the methods for different types of noise distributions. In addition, we also showed the outcome as a function of the distance from the true core (instead of taking 1.0 cm).

Bibliography

1. Albert-László Barabási. *Network science.* Cambridge University Press, 2016.
2. Sergey Brin and Lawrence Page. Reprint of: The anatomy of a large-scale hypertextual web search engine. *Computer networks*, 56(18):3825–3833, 2012.
3. H.W. Kroto, J.R. Heath, S.C. O'Brien, R.F. Curl, and R.E. Smalley. C_{60}: Buckminsterfullerene. *Nature*, 318(6042):162–163, 1985.
4. Stephen P Borgatti, Ajay Mehra, Daniel J Brass, and Giuseppe Labianca. Network analysis in the social sciences. *science*, 323(5916):892–895, 2009.
5. Albert-Laszlo Barabasi and Zoltan N Oltvai. Network biology: understanding the cell's functional organization. *Nature reviews genetics*, 5(2):101–113, 2004.
6. Albert-László Barabási, Natali Gulbahce, and Joseph Loscalzo. Network medicine: a network-based approach to human disease. *Nature Reviews Genetics*, 12(1):56–68, 2011.
7. Leon Danon, Ashley P Ford, Thomas House, Chris P Jewell, Matt J Keeling, Gareth O Roberts, Joshua V Ross, and Matthew C Vernon. Networks and the epidemiology of infectious disease. *Interdisciplinary perspectives on infectious diseases*, 2011, 2011.
8. Dirk Brockmann and Dirk Helbing. The hidden geometry of complex, network-driven contagion phenomena. *Science*, 342(6164):1337–1342, 2013.
9. Cornelis J Stam. Modern network science of neurological disorders. *Nature Reviews Neuroscience*, 15(10):683–695, 2014.
10. Milad El Haddad, Richard Houben, Rene Tavernier, and Mattias Duytschaever. Stable reentrant circuit with spiral wave activation driving atrial tachycardia. *Heart Rhythm*, 11(4):716–718, 2014.
11. Anshul M Patel, Andre d'Avila, Petr Neuzil, Steven J Kim, MSEE, Theofanie Mela, Jagmeet P Singh, Jeremy N Ruskin, and Vivek Y Reddy. Atrial tachycardia after ablation of persistent atrial fibrillation: identification of the critical isthmus with a combination of multielectrode activation mapping and targeted entrainment mapping. *Circulation: Arrhythmia and Electrophysiology*, 1(1):14–22, 2008.
12. Anthony G Brooks, Martin K Stiles, Julien Laborderie, Dennis H Lau, Pawel Kuklik, Nicholas J Shipp, Li-Fern Hsu, and Prashanthan Sanders. Outcomes of long-standing persistent atrial fibrillation ablation: a systematic review. *Heart Rhythm*, 7(6):835–846, 2010.
13. R Weerasooriya, P Khairy, J Litalien, L Macle, et al. Catheter ablation for atrial fibrillation: are results maintained at 5 years of follow-up? jacc 2011; 57: 160-166. 21. altman rk, proietti r, barett cd, perini ap et al. management of refractory atrial fibrillation post surgical ablation. *Ann Cardiothorac Surg*, 3(1):91–97, 2014.
14. James N Weiss, Zhilin Qu, and Kalyanam Shivkumar. Ablating atrial fibrillation: A translational science perspective for clinicians. *Heart rhythm*, 13:1868–1877, Sep 2016. ISSN 1556-3871. doi: 10.1016/j.hrthm.2016.05.026.
15. Nele Vandersickel, Alexandre Bossu, Jan De Neve, Albert Dunnink, Veronique MF Meijborg, Marcel AG van der Heyden, Jet DM Beekman, Jacques MT De Bakker, Marc A Vos, and Alexander V Panfilov. Short-lasting episodes of torsade de pointes in the chronic atrioventricular block dog model have a focal mechanism, while longer-lasting episodes are maintained by re-entry. *JACC: Clinical Electrophysiology*, 3(13):1565–1576, 2017.
16. Richard A Gray, Arkady M Pertsov, and José Jalife. Spatial and temporal organization during cardiac fibrillation. *Nature*, 392(6671):75, 1998.
17. Milad El Haddad, Richard Houben, Roland Stroobandt, Frederic Van Heuverswyn, Rene Tavernier, and Mattias Duytschaever. Algorithmic detection of the beginning and end of bipolar electrograms: implications for novel methods to assess local activation time during atrial tachycardia. *Biomedical Signal Processing and Control*, 8(6):981–991, 2013.
18. Sohail Zahid, Kaitlyn N Whyte, Erica L Schwarz, Robert C Blake, Patrick M Boyle, Jonathan Chrispin, Adityo Prakosa, Esra G Ipek, Farhad Pashakhanloo, Henry R Halperin, et al. Feasibility of using patient-specific models and the "minimum cut" algorithm to predict optimal ablation targets for left atrial flutter. *Heart Rhythm*, 13(8):1687–1698, 2016.
19. Susumu Tao, Samuel F Way, Joshua Garland, Jonathan Chrispin, Luisa A Ciuffo, Muhammad A Balouch, Saman Nazarian, David D Spragg, Joseph E Marine, Ronald D Berger, et al. Ablation as targeted perturbation to rewire communication network of persistent atrial fibrillation. *PloS one*, 12(7):e0179459, 2017.
20. S Zeemering, R Peeters, A van Hunnik, S Verheule, and U Schotten. Identification of recurring wavefront propagation patterns in atrial fibrillation using basis pursuit. In *Engineering in Medicine and Biology Society (EMBC), 2013 35th Annual International Conference of the IEEE*, pages 2928–2931. IEEE, 2013.
21. Tobias Georg Oesterlein, Axel Loewe, Gustavo Lenis, Armin Luik, C Schmitt, and Olaf Doessel. Automatic identification of reentry mechanisms and critical sites during atrial tachycardia by analyzing areas of activity. *IEEE Transactions on Biomedical Engineering*, 2018.
22. Bradley P Knight, Adam Zivin, Joseph Souza, Matthew Flemming, Frank Pelosi, Rajiva Goyal, K Ching Man, S Adam Strickberger, and Fred Morady. A technique for the rapid diagnosis of atrial tachycardia in the electrophysiology laboratory. *Journal of the American College of Cardiology*, 33(3):775–781, 1999.
23. Massimo Zoni-Berisso, Fabrizio Lercari, Tiziana Carazza, and Stefano Domenicucci. Epidemiology of atrial fibrillation: European perspective. *Clinical epidemiology*, 6:213, 2014.
24. Paulus Kirchhof, Stefano Benussi, Dipak Kotecha, Anders Ahlsson, Dan Atar, Barbara Casadei, Manuel Castella, Hans-Christoph Diener, Hein Heidbuchel, Jeroen Hendriks, Gerhard Hindricks, Antonis S Manolis, Jonas Oldgren, Bogdan Alexandru Popescu, Ulrich Schotten, Bart Van Putte, Panagiotis Vardas, Stefan Agewall, John Camm, Gonzalo Baron Esquivias, Werner Budts, Scipione Carerj, Filip Casselman, Antonio Coca, Raffaele De Caterina, Spiridon Deftereos, Dobromir Dobrev, José M Ferro, Gerasimos Filippatos, Donna Fitzsimons, Bulent Gorenek, Maxine Guenoun, Stefan H Hohnloser, Philippe Kolh, Gregory Y H Lip, Athanasios Manolis, John McMurray, Piotr Ponikowski, Raphael Rosenhek, Frank Ruschitzka, Irina Savelieva, Sanjay Sharma, Piotr Suwalski, Juan Luis Tamargo, Clare J Taylor, Isabelle C Van Gelder, Adriaan A Voors, Stephan Windecker, Jose Luis Zamorano, and Katja Zeppenfeld. 2016 esc guidelines for the management of atrial fibrillation developed in collaboration with eacts. *Europace : European pacing, arrhythmias, and cardiac electrophysiology : journal of the working groups on cardiac pacing, arrhythmias, and cardiac cellular electrophysiology of the European Society of Cardiology*, 18: 1609–1678, Nov 2016. ISSN 1532-2092. doi: 10.1093/europace/euw295.
25. Maurits Allessie and Natasja de Groot. Crosstalk opposing view: Rotors have not been demonstrated to be the drivers of atrial fibrillation. *The Journal of physiology*, 592:3167–3170, Aug 2014. ISSN 1469-7793. doi: 10.1113/jphysiol.2014.271809.
26. Sanjiv M Narayan and José Jalife. Crosstalk proposal: Rotors have been demonstrated to drive human atrial fibrillation. *The Journal of physiology*, 592:3163–3166, Aug 2014. ISSN 1469-7793. doi: 10.1113/jphysiol.2014.271031.
27. Maurits Allessie and Natasja de Groot. Rebuttal from Maurits Allessie and Natasja de Groot. *The Journal of physiology*, 592:3173, Aug 2014. ISSN 1469-7793. doi: 10.1113/jphysiol.2014.275404.
28. Sanjiv M Narayan and José Jalife. Rebuttal from Sanjiv M. Narayan and José Jalife. *The Journal of physiology*, 592:3171, Aug 2014. ISSN 1469-7793. doi: 10.1113/jphysiol.2014.275396.
29. Shih-Ann Chen, Flavia Ravelli, Michela Mase, Andreas Bollmann, Jedrzej Kosiuk, Gerhard Hindricks, John M. Miller, Michiel J. Janse, Riccardo Cappato, Michel Haissaguerre, Olivier Bernus, Remi Dubois, Igor Efimov, Ed Vigmond, Sanjay Dixit, and Kurt J. Schillinger. Comments on the crosstalk proposal and opposing view: Rotors have/have not been demonstrated to drive human atrial fibrillation. *Journal of Physiology*, 2015.
30. Sanjiv M. Narayan, David E. Krummen, Kalyanam Shivkumar, Paul Clopton, Wouter-Jan Rappel, and John M. Miller. Treatment of atrial fibrillation by the ablation of localized sources: Confirm (conventional ablation for atrial fibrillation with or without focal impulse and rotor modulation) trial. *Journal of the American College of Cardiology*, 60(7):628–636, Aug 2012.
31. Sanjiv M Narayan, Tina Baykaner, Paul Clopton, Amir Schricker, Gautam G Lalani, David E Krummen, Kalyanam Shivkumar, and John M Miller. Ablation of rotor and focal sources reduces late recurrence of atrial fibrillation compared with trigger ablation alone: extended follow-up of the confirm trial (conventional ablation for atrial fibrillation with or without focal impulse and rotor modulation). *Journal of the American College of Cardiology*, 63:1761–1768, May 2014. ISSN 1558-3597. doi: 10.1016/j.jacc.2014.02.543.
32. Carola Gianni, Sanghamitra Mohanty, Luigi Di Biase, Tamara Metz, Chintan Trivedi, Yalçın Gökoğlan, Mahmut F Güneş, Rong Bai, Amin Al-Ahmad, J David Burkhardt, G Joseph Gallinghouse, Rodney P Horton, Patrick M Hranitzky, Javier E Sanchez, Phillipp Halbfaß, Patrick Müller, Anja Schade, Thomas Deneke, Gery F Tomassoni, and Andrea Natale. Acute and early outcomes of focal impulse and rotor modulation (firm)-guided rotors-only ablation in patients with nonparoxysmal atrial fibrillation. *Heart rhythm*, 13:830–835, Apr 2016. ISSN

1556-3871. doi: 10.1016/j.hrthm.2015.12.028.

33. Sanghamitra Mohanty, Carola Gianni, Prasant Mohanty, Philipp Halbfass, Tamara Metz, Chintan Trivedi, Thomas Deneke, Gery Tomassoni, Rong Bai, Amin Al-Ahmad, Shane Bailey, John David Burkhardt, G Joseph Gallinghouse, Rodney Horton, Patrick M Hranitzky, Javier E Sanchez, Luigi Di Biase, and Andrea Natale. Impact of rotor ablation in nonparoxysmal atrial fibrillation patients: Results from the randomized oasis trial. *Journal of the American College of Cardiology*, 68:274–282, Jul 2016. ISSN 1558-3597. doi: 10.1016/j.jacc.2016.04.015.
34. Eric Buch, Michael Share, Roderick Tung, Peyman Benharash, Parikshit Sharma, Jayanthi Koneru, Ravi Mandapati, Kenneth A Ellenbogen, and Kalyanam Shivkumar. Long-term clinical outcomes of focal impulse and rotor modulation for treatment of atrial fibrillation: A multicenter experience. *Heart Rhythm*, 13(3):636–641, 2016.
35. Ramya Vijayakumar, Sunil K Vasireddi, Phillip S Cuculich, Mitchell N Faddis, and Yoram Rudy. Methodology considerations in phase mapping of human cardiac arrhythmias. *Circulation. Arrhythmia and electrophysiology*, 9, Nov 2016. ISSN 1941-3084. doi: 10.1161/CIRCEP.116.004409.
36. Pawel Kuklik, Stef Zeemering, Arne van Hunnik, Bart Maesen, Laurent Pison, Dennis H Lau, Jos Maessen, Piotr Podziemski, Christian Meyer, Benjamin Schaffer, Harry Crijns, Stephan Willems, and Ulrich Schotten. Identification of rotors during human atrial fibrillation using contact mapping and phase singularity detection: Technical considerations. *IEEE transactions on bio-medical engineering*, 64:310–318, Feb 2017. ISSN 1558-2531. doi: 10.1109/TBME.2016.2554660.
37. Stijntje D Roes, C Jan Willem Borleffs, Rob J van der Geest, Jos JM Westenberg, Nina Ajmone Marsan, Theodorus AM Kaandorp, Johan HC Reiber, Katja Zeppenfeld, Hildo J Lamb, Albert de Roos, et al. Infarct tissue heterogeneity assessed with contrast-enhanced mri predicts spontaneous ventricular arrhythmia in patients with ischemic cardiomyopathy and implantable cardioverter-defibrillatorclinical perspective. *Circulation: Cardiovascular Imaging*, 2(3):183–190, 2009.
38. Douglas R White and Stephen P Borgatti. Betweenness centrality measures for directed graphs. *Social Networks*, 16(4):335–346, 1994.
39. Ann E Sizemore, Chad Giusti, Ari Kahn, Jean M Vettel, Richard F Betzel, and Danielle S Bassett. Cliques and cavities in the human connectome. *Journal of computational neuroscience*, 44(1):115–145, 2018.
40. Petter Holme. Modern temporal network theory: a colloquium. *The European Physical Journal B*, 88(9):1–30, 2015.
41. Mark Newman. Networks: an introduction. 2010. *United Slates: Oxford University Press Inc., New York*, pages 1–2.
42. K. H W J ten Tusscher and A. V. Panfilov. Alternans and spiral breakup in a human ventricular tissue model. *Am J Physiol Heart Circ Physiol*, 291(3):H1088–H1100, Sep 2006. doi: 10.1152/ajpheart.00109.2006.
43. Nele Vandersickel, Ivan V Kazbanov, Anita Nuitermans, Louis D Weise, Rahul Pandit, and Alexander V Panfilov. A study of early afterdepolarizations in a model for human ventricular tissue. *PloS one*, 9(1):e84595, 2014.
44. Kirsten H W J Ten Tusscher, Rok Hren, and Alexander V Panfilov. Organization of ventricular fibrillation in the human heart. *Circulation Research*, 100(12):e87–101, Jun 2007.
45. K. H W J Ten Tusscher and A. V. Panfilov. Reentry in heterogeneous cardiac tissue described by the luo-rudy ventricular action potential model. *American Journal of Physiology-Heart and Circulatory Physiology*, 284(2):H542–H548, Feb 2003. doi: 10.1152/ajpheart.00608.2002.
46. Natasja MS de Groot, Richard PM Houben, Joep L Smeets, Eric Boersma, Ulrich Schotten, Martin J Schalij, Harry Crijns, and Maurits A Allessie. Electropathological substrate of longstanding persistent atrial fibrillation in patients with structural heart diseaseclinical perspective. *Circulation*, 122(17):1674–1682, 2010.
47. Bruno Taccardi, Bonnie B Punske, Frank Sachse, Xavier Tricoche, Piero Colli-Franzone, Luca F Pavarino, and Christine Zabawa. Intramural activation and repolarization sequences in canine ventricles. experimental and simulation studies. *Journal of electrocardiology*, 38 (4):131–137, 2005.
48. Madison S Spach, Walter T Miller, Elizabeth Miller-Jones, Robert B Warren, and Roger C Barr. Extracellular potentials related to intracellular action potentials during impulse conduction in anisotropic canine cardiac muscle. *Circulation Research*, 45(2):188–204, 1979.
49. Madison S Spach and Paul C Dolber. Relating extracellular potentials and their derivatives to anisotropic propagation at a microscopic level in human cardiac muscle. evidence for electrical uncoupling of side-to-side fiber connections with increasing age. *Circulation research*, 58(3):356–371, 1986.
50. Jan Pooter, Milad El Haddad, Michael Wolf, Thomas Phlips, Frederic Heuverswyn, Liesbeth Timmers, René Tavernier, Sebastien Knecht, Yves Vandekerckhove, and Mattias Duytschaever. Clinical assessment and comparison of annotation algorithms in high-density mapping of regular atrial tachycardias. *Journal of cardiovascular electrophysiology*, 29(1): 177–185, 2018.
51. KT Konings, CJ Kirchhof, JR Smeets, HJ Wellens, Olaf C Penn, and Maurits A Allessie. High-density mapping of electrically induced atrial fibrillation in humans. *Circulation*, 89(4): 1665–1680, 1994.
52. Mark-Anthony Bray and John P. Wikswo. Considerations in phase plane analysis for nonstationary reentrant cardiac behavior. *Phys. Rev. E*, 65:051902, May 2002.
53. M. A. Bray and J. P. Wikswo. Use of topological charge to determine filament location and dynamics in a numerical model of scroll wave activity. *IEEE Transactions on Biomedical Engineering*, 49(10):1086–1093, Oct 2002. ISSN 0018-9294. doi: 10.1109/TBME.2002.803516.
54. Mark-Anthony Bray, Shien-Fong Lin, Rubin R. Aliev, Bradley J. Roth, and John P. Wikswo. Experimental and theoretical analysis of phase singularity dynamics in cardiac tissue. *Journal of Cardiovascular Electrophysiology*, 12(6):716–722, 2001.
55. Karthikeyan Umapathy, Krishnakumar Nair, Stephane Masse, Sridhar Krishnan, Jack Rogers, Martyn P Nash, and Kumaraswamy Nanthakumar. Phase mapping of cardiac fibrillation. *Circulation: Arrhythmia and Electrophysiology*, 3(1):105–114, 2010.
56. Naoki Tomii, Masatoshi Yamazaki, Tatsuhiko Arafune, Haruo Honjo, Nitaro Shibata, and Ichiro Sakuma. Detection algorithm of phase singularity using phase variance analysis for epicardial optical mapping data. *IEEE Transactions on Biomedical Engineering*, 63(9): 1795–1803, 2016.
57. Enid Van Nieuwenhuyse, Gunnar Seemann, Alexander V Panfilov, and Nele Vandersickel. Effects of early afterdepolarizations on excitation patterns in an accurate model of the human ventricles. *PloS one*, 12(12):e0188867, 2017.
58. R Core Team. *R: A Language and Environment for Statistical Computing*. R Foundation for Statistical Computing, Vienna, Austria, 2017.
59. B Thomas Lumley, V. J. C. P. & Ripley. *gee: Generalized Estimation Equation Solver*, 2015. R package version 4.13-19.

Supplementary material

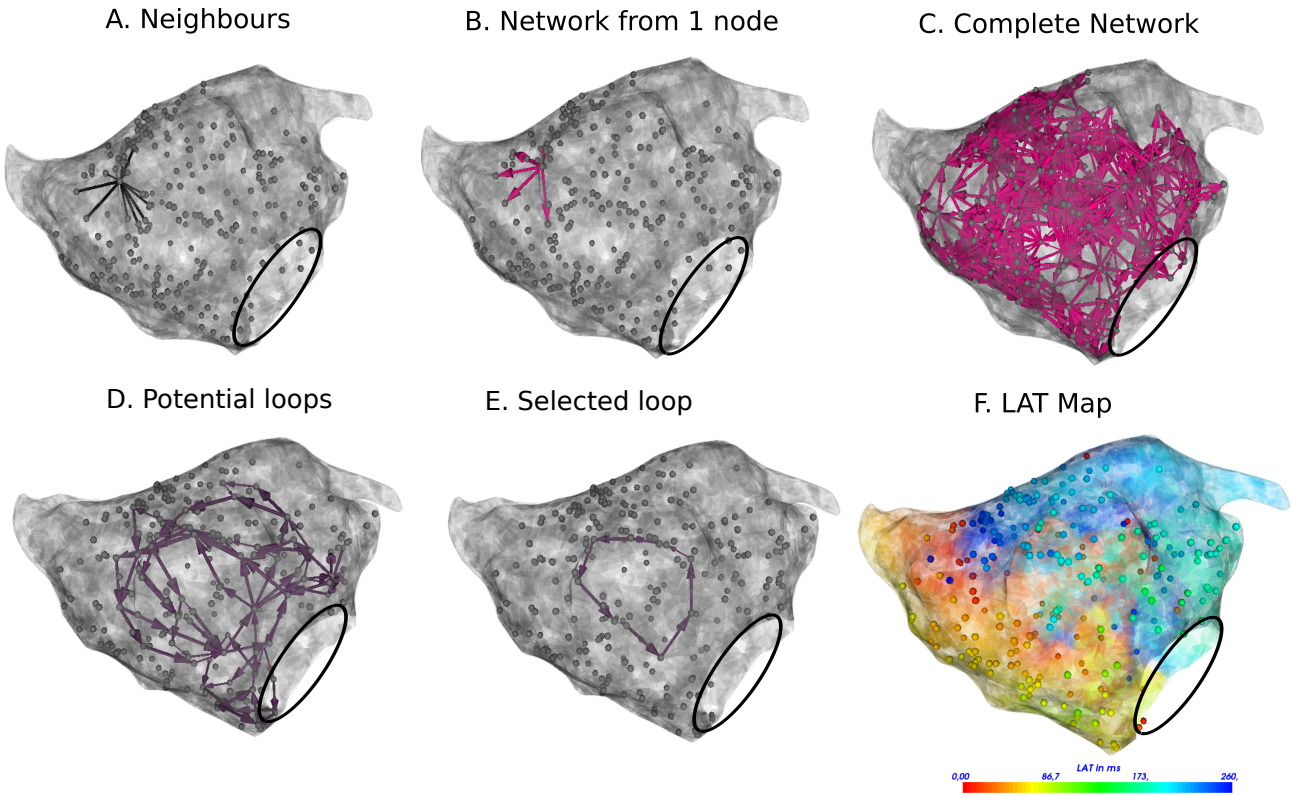

Fig. S1. DG-mapping for a regular AT case of localized reentry. The gray dots represent the mapping points, while the black circle denotes the mitral valve. Panel A shows an example of all possible neighbours for a single annotated location. Panel B represents the corresponding network for the same single annotated location. In Panel C the complete network is drawn from which all detected loops in the network are derived, see panel D. The selected loop among the bundle is shown in panel E. The LAT annotation map in ms is given in panel F.

#	code	# el	CL	Mechanism LAT map CARTO (EP)	Mechanism DG
1	ATM1	865	250	**Macro reentry**: perimitral circuit clockwise	✓
2	ATM2	784	300	Hypothesis 1: Large macro reentrant circuit sticking close to the right veins, traveling up on the anterior wall, over the roof and down on the posterior wall. There is a SCC on the anterior RSPV side. Hypothesis 2: **localized reentry** circuit at the anterior wall next to the RSPV through the SCC ablation was done on the SCC, which agrees with both hypothesis.	✓(hypothesis 2)
3	ATM3	219	450	Hypothesis 1: Large **macro reentry**: roof traveling up on the anterior wall, over the roof and down on the posterior wall. Hypothesis 2: localized reentry on the anterior wall.	✓(hypothesis 1)
4	ATM4	1722	225	Double loop: **macro reentry**: perimitral reentry counterclockwise and **macro reentry** around the LV over the roof.	✓
5	ATM5	1567	200	**Macro reentry**: perimitral reentry clockwise	✓
6	ATM6	1752	214	Hypothesis 1: double loop: **macro reentry**: perimitral counterclockwise and **macro reentry** around the LV over the roof. Hypothesis 2: roof dependent macro reentry, with a pseudo (slower) reentry around the mitral valve.	Only perimitral counterclockwise reentry found but the ablation target would be at the same location ☑

7	PC1	1753	245	**Focal**	✓(no loops detected)
8	PC2	889	290	**Macro reentry**: roof	✓
9	PC3	896	302	**Macro reentry**: perimitral reentry clockwise	✓
10	PC4	431	240	Perimitral circuit counterclockwise. This was ablated and the AT changed and switched through the roof with a CL of 228 ms. However, retrospective offline analysis revealed a localized reentry below the left atrial appendage (at the base of the LAA). Original ablation points agree with localized reentry.	✓(localized-reentry)
11	PC5	847	250	**Macro reentry**: peritricuspid reentry in the right atrium	✓
12	PC6	444	278	**Macro reentry**: mitral reentry counterclockwise	✓
13	PC7	354	340	**Macro reentry:** perimitral circuit	✓
14	PC8	938	260	**Macro reentry**: perimitral circuit counterclockwise and a second loop going through the roof. The two loops are merging at the left veins.	Only perimitral reentry found but the ablation target would be at the same location ☑
15	PC9	283	304	**Focal**	✓(no loops detected)
16	PC10	3524	240	The online LAT map was uninterpretable, however roof line ablation was performed. Offline retrospective re-evaluation showed a possible atypical focal activity from the scar on the roof. The ablation roof line went through that scar and that possible terminated the AT.	✓(no loops detected)
17	CD201	475	260	Localized **localized reentry** at the crosspoint at the appendage and the roof, anterior superior appendage from the left atrium.	✓
18	CD203	1092	240	Localized **localized reentry** at the anterior wall near the mitral annulus at 11 o' clock.	✓
19	CD204	1091	240	Hypothesis 1: **macro reentry**: perimitral circuit counterclockwise using a SCC in between the mitral anulus at 10 o'clock and a scar at the anterior wall. Hypothesis 2: the same loop as in hypothesis 1, but a second loop is found through the same SCC turning around the scar at the anterior wall. Ablation at the SCC terminated the AT (according to hp1).	✓ (hypothesis 1)
20	CD205	463	290	Hypothesis 1: **macro reentry**: perimitral circuit clockwise using a SCC in between the mitral annulus at 10'o clock and a scar at the anterior wall. Hypothesis 2: the same loop as in hypothesis 1, but a second loop through the same SCC turning around the scar at the anterior wall counterclockwise. (the size of this second loop cannot be determined). Ablation at the SCC terminated the AT (according to hypothesis 1)	✓ (hypothesis 1).
21	CD206a	612	250	**Focal** breakthrough at the septum inferior and right inferior PV.	✓(no loops detected)
22	CD206b	360	250	**Focal** AT at posterior septum superior, but 2 signals were not able to be explained by the focal activity. After diagnosis from DG-mapping, the map was reconsidered and localized reentry agreed better with the map.	**Localized reentry** at the posteral septal wall but the ablation target would be at the same location ☑
23	CD207	648	215	**Macro reentry**: clockwise mitral valve	✓

24	CD208	876	315	Hypothesis 1: **Macro reentry** circuit at the septum anterior from the right superior pulmonary vain, active or passive. Hypothesis 2: Same loop as in hypothesis 1, but it might be passive because of another loop with the same pathway that turns around the left veins through the mitral isthmus, coming back over the roof. Ablation at the roof terminated the AT.	✓(hypothesis 1)
25	CD209	489	270	**Macro reentry**: roof ascending over the anterior wall and descending over the posterior wall.	✓
26	CD210	628	340	**Localized reentry** at the septum	✓
27	CD211	603	210	Hypothesis 1: **Localized reentry** or might be larger reentry at the anterior wall near the mitral annulus at 11 o'clock anterior from the LAA. Hypothesis 2: Counterclockwise perimitral circuit: less likely because of colliding wavefront. EP treated as hypothesis 1.	✓(hypothesis 1)
28	CD212a	1147	250	Hypothesis 1: **Macro reentry** tachycardia roof dependent, ascending on the anterior wall, descending on posterior wall, collision on posterior mitral isthmus. Hypothesis 2: it could be a smaller loop clockwise around perimitral.	✓(hypothesis 1)
29	CD212b	1089	285	**Macro reentry**: clockwise mitral valve	✓
30	CD213	1322	305	There is a SCC at the roof near the RV (there is a gap in a prior ablation line). Hypothesis 1: through SCC a large **macro reentry**: around the RV. Hypothesis 2: through SCC, more localized reentrant circuit using a second gap at the roof for reentry. Hypothesis 3: Both hypothesis might be correct (i.e. double loop). EP ablated at the SCC at the roof, according to hypothesis 1. EP ablated at the SCC at the roof, according to hypothesis 1.	✓(hypothesis 1)
31	CD214	439	305	**Macro reentry**: perimitral reentry clockwise pushed away from the mitral annulus (Y shape).	✓

Table S1. Summary of the 31 clinical cases of regular AT. For cases 1-16, we used non-interpolated data given by the CARTO system. For cases 17-32, the interpolated data from CARTO was used. The columns represent the case number (#), the database code, the number of measured points (# el), the cycle length (CL), the mechanism found by the EP and the mechanism found by DG-mapping. We put a ✓if the mechanism fully agrees, and a ☑ if the ablation point agrees, but a different mechanism is seen. SCC = slow conductive channel, PV = pulmonary vain, RSPV = right superior pulmonary vain, RV = right vain, LAA = Left Anterior Appendage.

	64				256			
	0.5		1		0.5		1	
σ	PM	DG	PM	DG	PM	DG	PM	DG
0	100	100	100	100	100	100	100	100
5	73	45	92	96	68	98	74	100
10	46	40	75	91	49	95	62	100
15	26	35	51	83	19	83	30	95
20	9	27	21	68	0	62	1	81
25	2	18	6	50	0	40	0	60
30	1	12	2	34	0	24	0	41

Table S2. Percentage of correct cores as a function of increasing noise (i.e. increasing standard deviation σ of the Gaussian noise) for varying radius to the true core (0.5 or 1 cm) and a varying number of electrodes (64 or 256). PM stands for phase mapping and DG for DG-mapping. DG-mapping outperforms phase mapping except for a radius of 0.5 cm with 64 electrodes.

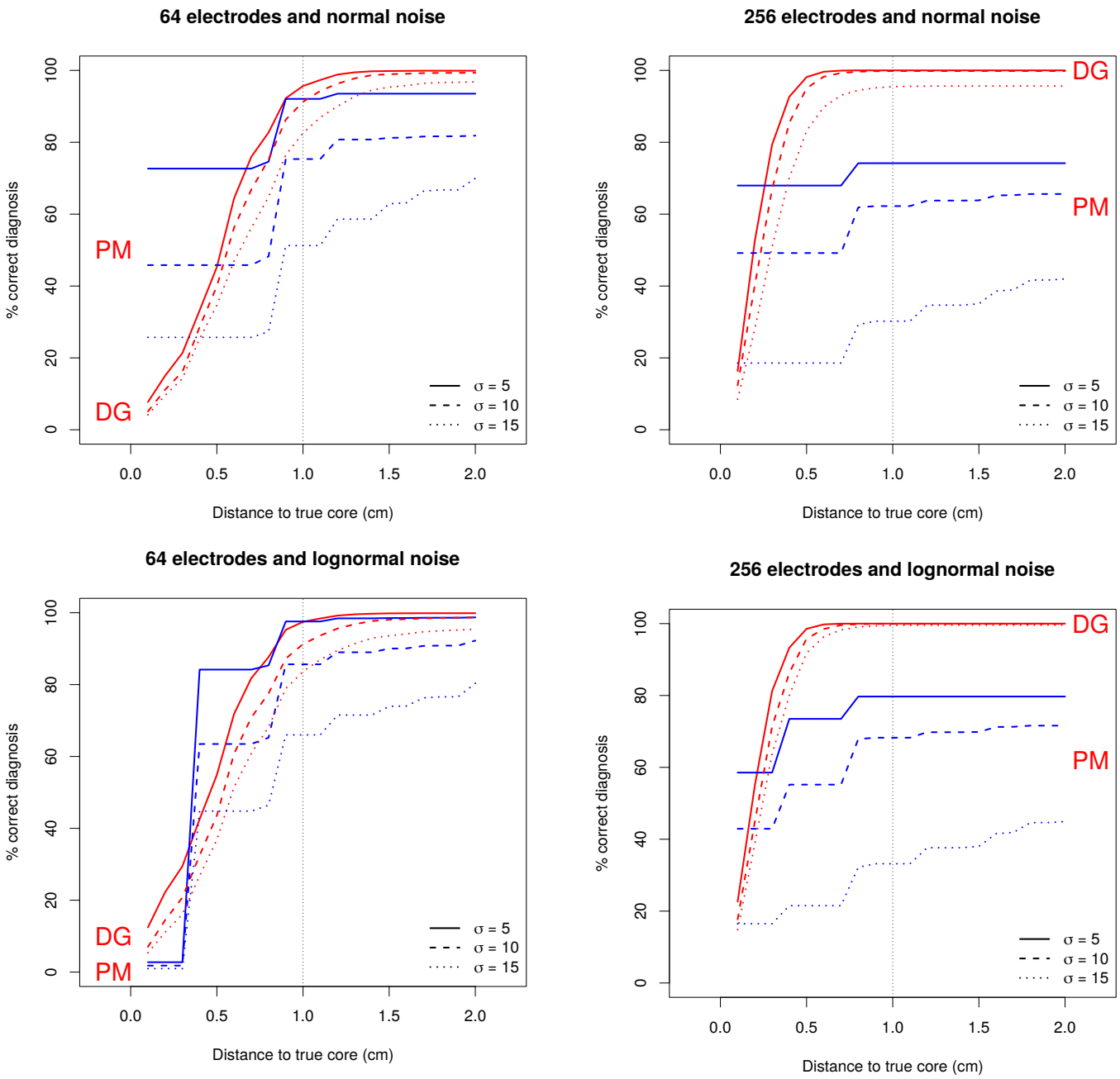

Fig. S2. Percentage of correct diagnoses as a function of distance to the true core for different levels of the standard deviation of the noise σ. The red lines denote DG-mapping the blue lines phase mapping (PM). The top panels show the performance for normal noise, while for the bottom panels the noise follows a lognormal distribution. DG-mapping has a continuous behavior, while phase mapping shows a stepwise behavior. This is because phase mapping has a resolution determined by the size of the smallest square in the tissue (16x16 mm for the 64 electrode grid, 8x8 mm for the 265 electrode). The minimal steps in performance are seen each 8 mm for 64 electrodes and 4 mm for 265 electrodes, which agrees with the difference of the center of one square and the average of the centers of two contiguous squares, as shown in Figure S3. Therefore, the minimal step in accuracy for phase mapping is determined by the grid size. Phase mapping and DG-mapping can only be compared above this minimal accuracy. The graphs display a superior performance of DG-mapping over phase mapping for both normal and lognormal noise, for all choices of σ and for distances to the true core exceeding 1 cm. Overall, the performance of DG-mapping is similar for normal and lognormal noise and improves with increasing number of electrodes.

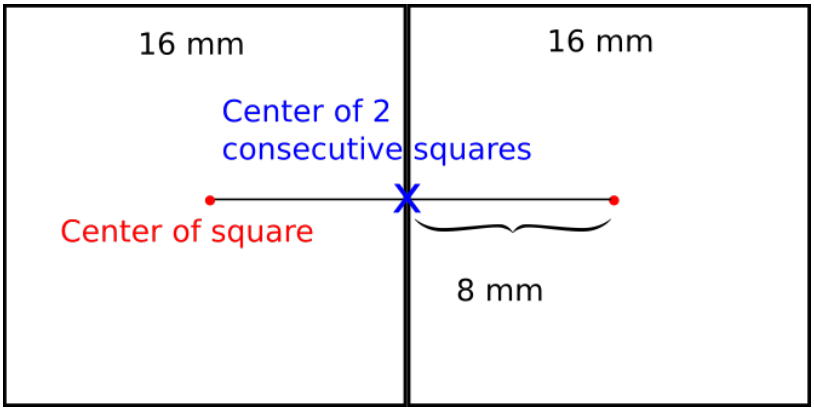

Fig. S3. Minimal distance between the center of a square and two consecutive squares for 64 electrodes.